Check for updates

MATERIALS SCIENCE

Heterogeneous integration of ultrawide bandgap semiconductors for radio frequency power devices

Hong Zhou[1], Min Zhou[1]*, Mingjie Xiang[1], Hehe Gong[2,3], Guangjie Gao[1], Chenlu Wang[1], Yachao Zhang[1], Kui Dang[1], Zhihong Liu[1], Jinfeng Zhang[1], HangMing Zhang[3], Yifan Wang[2], Han Wang[3], Mengwei Si[4], Yuhao Zhang[3]*, Yue Hao[1], Jincheng Zhang[1]*

Copyright © 2025 The Authors, some rights reserved; exclusive licensee American Association for the Advancement of Science. No claim to original U.S. Government Works. Distributed under a Creative Commons Attribution License 4.0 (CC BY).

Ultrawide bandgap (UWBG) semiconductors offer high critical electric fields and saturation velocities ideal for radio frequency (rf) devices, but achieving both shallow-level doping and high thermal conductivity (k_T) in a single material remains difficult. We demonstrate a scalable, exfoliation-based layer-transfer process to heterogeneously integrate gallium oxide (Ga_2O_3) thin films with shallow dopants onto high-k_T aluminum nitride (AlN) substrates. This method obviates ion implantation and interfacial dielectric layers used in conventional approaches. A large conduction band offset (3.4 electron volts) at the Ga_2O_3/AlN interface improves electron confinement in the Ga_2O_3 channel. T-gate rf power transistors achieve a maximum oscillation frequency of 90 gigahertz and output power densities of 4.6 watts per millimeter at 2 gigahertz and 4.1 watts per millimeter at 6 gigahertz—among the highest for UWBG devices. A minimal noise figure of 0.48 decibels at 8 gigahertz—among the lowest reported in this frequency range—further highlights the platform's promise for next-generation rf applications.

INTRODUCTION

Radio frequency (rf) semiconductor devices are used ubiquitously in applications like telecommunication, consumer electronics, aerospace, defense, and health care, with a global market over \$23 billion (https://fortunebusinessinsights.com/rf-semiconductor-market-110167). The overarching design target of many rf devices is to concurrently achieve high cutoff frequency (f_T) and maximum oscillation frequency (f_{max}), high output power density (P_{out}), high efficiency, low noise, and high linearity. The frequency and power performance of rf devices can be substantially boosted by deploying wide bandgap (WBG) and ultrawide bandgap (UWBG) semiconductors, due to their superior properties including large bandgap, high critical electric field (E_C), and high saturation velocity (ν_{sat}) (*1*, *2*). The past two decades have witnessed the commercialization of WBG gallium nitride (GaN) rf power devices with a market size over \$740 million (*3*). On the horizon, UWBG semiconductors such as gallium oxide (Ga_2O_3), aluminum nitride (AlN), boron nitride, and diamond promise a superior performance limit for rf devices (*4*). For example, the Johnson figure-of-merit ($JFOM = E_C^2 \times \nu_{sat}^2/4\pi^2$), a widely used material indicator for rf device performance, is three times higher in Ga_2O_3 compared to GaN (*5*, *6*).

In addition to E_C and ν_{sat}, the availability of shallow-level dopant and high thermal conductivity (k_T) are also crucial to rf devices. The deep-level dopant can limit the device's breakdown voltage (BV) and current density (*7*), and low k_T results in high junction temperature, both limiting the device power capacity. In addition, the relatively slow ionization of deep-level dopant could also limit the device switching frequency (*8*). Unfortunately, shallow dopants and low k_T are very challenging or even impossible to achieve in a single UWBG material (*2*). For example, Ga_2O_3 is known to offer shallow donors, large-area wafer, and a decent electron mobility, but it suffers a very low k_T that is only 1/6 of Si, 1/10 of GaN, and 1/20 of SiC (*5*). On the other hand, AlN and diamond have a high k_T but lack shallow-level dopants (*2*). Such material properties limit the rf device performance. For example, the state-of-the-art Ga_2O_3 rf transistors, despite having achieved a f_T of 10 to 27 GHz and f_{max} of 24 to 55 GHz (*9*–*11*), exhibit a limited P_{out} below 0.715 W/mm (*12*–*14*), which is much lower than the GaN counterpart.

A promising solution to the above challenge is combining the complementary properties of distinct UWBG materials through heterogeneous integration. To address the thermal limitation of Ga_2O_3, integration of Ga_2O_3 thin films on a variety of substrates including Si (*15*, *16*), SiC (*15*–*19*), GaN (*20*), and diamond (*21*–*24*) have been recently demonstrated. These integrations are primarily based on three approaches: (i) mechanical exfoliation and layer transfer (*20*–*22*, *24*, *25*), (ii) hydrogen (H) implantation–based ion cutting (*15*, *16*, *18*, *26*), and (iii) wafer fusion bonding (*17*, *23*, *27*, *28*). The Ga_2O_3-on-SiC rf transistors fabricated by ion implantation and bonding process have achieved a high P_{out} of 2.3 W/mm at $f = 4$ GHz (*19*), about three times higher than the best report on Ga_2O_3-on-Ga_2O_3.

However, the performance of Ga_2O_3-on-SiC rf transistors is still far from what the Ga_2O_3 material can provide, mainly due to several challenges facing the current heterogeneous integration techniques. First, the flakes produced in mechanical exfoliation usually have a size limited to submicrometers and highly uncontrollable, preventing the fabrication of large-area devices and microwave integrated circuits. Second, the ion cutting technique usually requires H implantation across the active device layer and high-temperature annealing, which can degrade the channel material (*29*). Third, many bonding techniques require an interfacial amorphous layer, which usually has a poor k_T. Such a layer has been reported to generate an effective thermal boundary resistance up to 60 m^2K/GW (*16*, *17*), accounting for up to 20% of the device's total thermal resistance (R_T). Last, the E_C of many host substrates (e.g., SiC) or interfacial layer is much lower than the channel material, leading to premature breakdown.

In this work, we develop a distinct heterogeneous integration technique that combines mechanical exfoliation, arrayed transfer,

[1]State Key Laboratory of Wide-Bandgap Semiconductor Devices and Integrated Technology, School of Microelectronics and Guangzhou Institute of Technology, Xidian University, Xi'an 710071, China. [2]Center for Power Electronics Systems, Virginia Tech, Blacksburg, VA 24060, USA. [3]Department of Electronic and Electrical Engineering and Centre for Advanced Semiconductors and Integrated Circuits, University of Hong Kong, Hong Kong, China. [4]Department of Electronic Engineering, Shanghai Jiao Tong University, Shanghai 200240, China.
*Corresponding author. Email: minzhou@stu.xidian.edu.cn (M.Z.); yuhzhang@hku.hk (Y.Z.); jchzhang@xidian.edu.cn (J.Z.)

Downloaded from https://www.science.org at Shanghai Jiao Tong University on May 12, 2026

and wafer-level direct bonding. The Ga_2O_3 films are cleaved from the edge of a Ga_2O_3 substrate, ensuring a good uniformity of film size. These films are then transferred onto a substrate and placed in an array, followed by a wafer-level room-temperature bonding that reduces the thickness nonuniformity of the arrayed films. This method obviates the ion implantation, interfacial oxide, and high-temperature annealing required in many conventional heterogeneous integration approaches. The relatively good uniformity in geometries and thickness effectively upscales the total size of the exfoliated film arrays to the wafer scale, enabling the fabrication of large-area electronics such as interconnected devices and integrated circuits.

In addition, different from the Si and SiC substrates used in prior Ga_2O_3 integration studies, we select the AlN substrate, which offers a high k_T of ~3 W/(cm·K) and a high E_c up to 10 MV/cm (*30*) as well as a favorable band alignment to Ga_2O_3. Because of the ultralow electron affinity (0.6 eV) of AlN (*30*), a 3.4-eV high barrier forms at the Ga_2O_3/AlN interface, which is 2.5 eV higher than the Ga_2O_3-SiC interface. This barrier can enhance electron confinement in the thin Ga_2O_3 channel and favors the gate scaling in rf transistors. Leveraging these process and material innovations, the fabricated Ga_2O_3-on-AlN rf transistor sets performance records for f_{max}, P_{out}, and power-added efficiency (PAE) in UWBG rf devices. The average electric field and noise level is among the best in rf devices reported in all material systems, verifying the high material quality in this hetero-UWBG platform.

RESULTS AND DISCUSSION

Heterogeneous integration and material characterization

Figure 1A illustrates the heterogeneous integration process developed in this work. The monoclinic β-Ga_2O_3 is the most thermally stable phase of Ga_2O_3, and the single-crystal β-Ga_2O_3 substrate are available up to 6-inch in the industry (*31*). β-Ga_2O_3 has a large lattice constant of 12.2 Å along the (100) orientation, allowing the β-Ga_2O_3 thin film to be easily cleaved and transferred on the blue tape. Distinct from the planar exfoliation widely adopted in prior works, here we exfoliate Ga_2O_3 thin films from the edge of a 2-inch (-201) n-Ga_2O_3 substrate grown via the edge-defined film-fed growth (EFG). The substrate has an n-type doping concentration (N_D) of 8×10^{18} cm^{-3} and a thickness of 500 μm. As the width of exfoliated film is determined by the substrate thickness, a consistent geometry around 5000 μm by 500 μm are produced in the repeated exfoliation. Subsequently, these exfoliated belts are placed in an array with a uniform belt-to-belt spacing, with the total array size scalable to the wafer level.

After the array formation, the β-Ga_2O_3 layer needs to be thinned down from tens of micrometers to below 500 nm for rf device fabrication. This is realized by multiple rounds of wafer-scale direct bonding at room temperature, which guarantees uniform bonding force across the wafer; the process details are elaborated in Materials and Methods. After reaching the target film thickness, β-Ga_2O_3 thin films are transferred from the carrier blue tape to a single-crystal 1-inch AlN substrate by a final bonding with a higher force and longer time. Figure 1B shows the optical microscopic images of a β-Ga_2O_3 belt transferred onto the AlN wafer. Figure 1C shows the thickness mapping of the 120 β-Ga_2O_3 belts across the wafer, revealing an average thickness of 428 nm with an SD of 123 nm. Photos of the key steps of this process are presented in fig. S1. Note that the Ga_2O_3 belt thickness uniformity may be further increased by the chemical-mechanical-planarization (CMP) process or choosing a thicker Ga_2O_3 crystal ingot, which can provide a more uniform Ga_2O_3 belt.

Table S1 of the Supplementary Materials compares this approach with three prior methods for heterogeneous integration—Scotch tape–based exfoliation, ion cutting, and fusion bonding. Here, the implantation-free, interfacial oxide-free approach with wafer-level scalability can potentially offer superior electrical and thermal properties for rf power devices. It can also be widely applicable to other van der Waals materials for heterogeneous integration. To showcase this applicability, we also fabricate Ga_2O_3 arrayed belts on the Si/SiO_2 substrate and SiC substrate by the same process, which will be used as control samples in electrical and thermal characterizations.

As shown in Fig. 1D, the surface root mean square (RMS) roughness of β-Ga_2O_3 surface is 0.2 nm. Figure 1E shows the high-resolution transmission electron microscopy (HRTEM) image of the bonded AlN/Ga_2O_3 interface. The abrupt interface further confirms the absence of an interfacial dielectric layer. The Al, N, Ga, and O elements are confirmed by the energy-dispersive x-ray spectroscopy (EDX) mapping at the interface, as presented in fig. S2. As shown in Fig. 1F, x-ray diffraction (XRD) characterization of the β-Ga_2O_3 on AlN only reveals a sharp Ga_2O_3 peak and AlN peak, suggesting the absence of an interfacial material. Figure 1G shows the high-resolution rocking curve of the bonded β-Ga_2O_3 on AlN reveals a narrow full width at half maximum (FWHM) of 80 arc sec, verifying the high quality of the transferred β-Ga_2O_3.

Device fabrication and thermal characterization

A mesa-shaped test device is first used to compare the voltage blocking capabilities of the fabricated Ga_2O_3-on-SiC and Ga_2O_3-on-AlN wafers (Fig. 2A). The *BV* between two electrodes with a spacing of 4 μm increases from 475 V in Ga_2O_3-on-SiC to 1230 V in Ga_2O_3-on-AlN, rendering a three times higher average electric field up to 3 MV/cm. This comparison illustrates the enhanced voltage blocking capabilities of the full-UWBG Ga_2O_3-on-AlN platform benefiting from the high E_C of the AlN substrate.

In addition to a higher breakdown field, the AlN substrate also enables superior electron confinement in the Ga_2O_3 channel. Figure 2B compares the band alignment diagram of the Ga_2O_3/SiC and Ga_2O_3/AlN heterojunctions. Benefiting from the low electron affinity of AlN, the Ga_2O_3/AlN junction provides a conduction band discontinuity of 3.4 eV, which is 2.5 eV higher than the Ga_2O_3/SiC junction. This high-potential back barrier can effectively suppress the channel carrier spill over and enhance the gate control over channel electrostatics. Such an enhanced gate control further allows for downscaling the gate length and increasing the channel doping, which improves f_T/f_{max} and on-state current, respectively.

Figure 2C shows the three-dimensional schematic of the T-gate rf transistor fabricated on the Ga_2O_3-on-AlN wafer. A high N_D of 8×10^{18} cm^{-3}, which is the N_D of the n$^+$-Ga_2O_3 substrate in the host wafer, is adopted for the n-Ga_2O_3 channel. A recessed T-gate reduces the channel thickness below the gate, which suppresses the short-channel effect (SCE), and forms a field plate structure in the gate-to-drain access region, which enhances the device *BV*. Top-view and cross-sectional scanning electron microscopy (SEM) images of the fabricated β-Ga_2O_3 rf power metal oxide semiconductor field-effect transistor (MOSFET) are displayed as Fig. 2D, with the fabrication process detailed in the Materials and Methods section. Devices with various gate length (L_G) and gate-to-drain distance (L_{GD}) are fabricated. Devices with a $L_G/L_{GD}/L_{GS}$ = 300/700/400 nm are used for rf

Downloaded from https://www.science.org at Shanghai Jiao Tong University on May 12, 2026

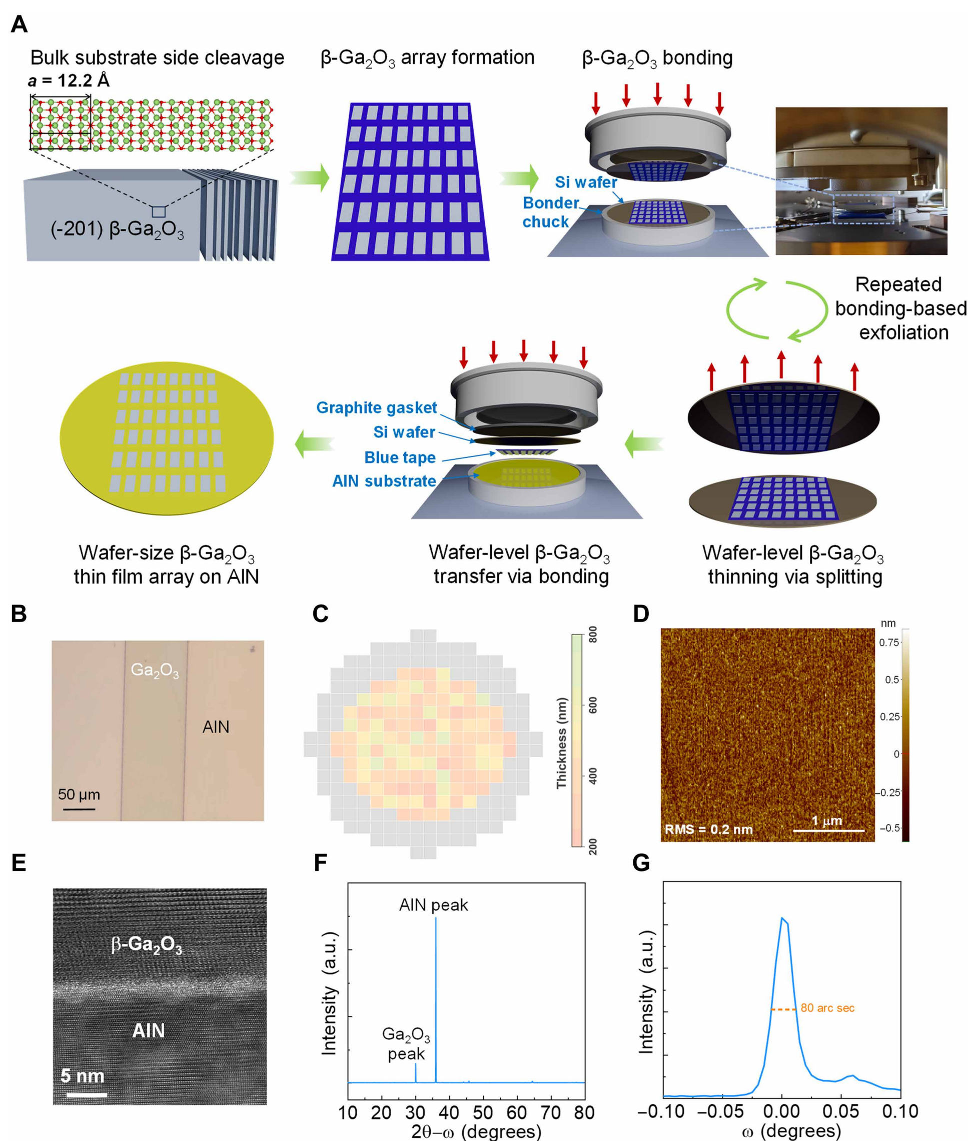

Fig. 1. Heterogeneous integration process and material characterization. (**A**) Illustration of the Ga_2O_3/AlN heterogeneous integration process. The β-Ga_2O_3 belt or film with uniform geometry is cleaved from the substrate edge and then manually transferred onto the blue tape to form an array. The thickness of β-Ga_2O_3 films on blue tape is reduced by multiple wafer-level bonding process until the thickness reaches around 500 nm. The graphite/Si/β-Ga_2O_3/AlN stack is formed and loaded into the bonding chamber under a 3-hour bonding process to transfer the wafer-size β-Ga_2O_3 film array onto the AlN substrate. (**B**) Top-view optical microscopic image of part of a single β-Ga_2O_3 film on the AlN substrate. (**C**) Thickness mapping of 120 β-Ga_2O_3 films in a wafer-size array after being transferred onto the 1-inch AlN substrate. (**D**) Atomic force microscopy (AFM) image of the surface of β-Ga_2O_3 film transferred on the AlN substrate, revealing an atomic flat surface with an RMS roughness of 0.2 nm. (**E**) Zoomed-in and HRTEM image at the atomic interface between the β-Ga_2O_3 channel and AlN substrate. (**F**) XRD scan characteristics of β-Ga_2O_3 on AlN. a.u., arbitrary units. (**G**) High-resolution rocking curve of transferred and bonded β-Ga_2O_3 with an FWHM of 80 arc sec.

power, noise, and linearity characterizations, whereas devices with a further scaled $L_G = 150$ nm and $L_{GD} = 700$ nm are used for the microwave noise measurements. Additional devices with a long L_G of 1 and 30 μm are used for thermal resistance (R_T) and channel mobility measurements, respectively. From the transfer characteristic of the long-channel device, the electron mobility and density in the recessed Ga_2O_3 channel is extracted to be ~80 cm^2/Vs and 1×10^{13} ~ 1.9×10^{13} cm^{-2}, respectively, as shown in fig. S3.

The R_T of the fabricated Ga_2O_3-on-AlN, Ga_2O_3-on-Si/SiO_2 and Ga_2O_3-on-SiC devices are measured by a transient thermal reflectance method, with the details described in the Materials and Methods section. As shown in Fig. 2E, the R_T of the Ga_2O_3-on-AlN device is measured to be 3.9 mm·K/W across a wide range of P_{out}, which is similar to the R_T of Ga_2O_3-on-SiC device and over three times lower than that of the Ga_2O_3-on-Si/SiO_2 device. Compared with other homogeneous or heterogeneously integrated Ga_2O_3 transistors reported in the literature (*17*, *26*, *32*–*38*), our Ga_2O_3-on-AlN device demonstrates one of the lowest R_T, as shown in Fig. 2F. This performance is ascribed to the ultrathin Ga_2O_3 layer, high-k_T substrate, and the absence of the low-k_T interfacial bonding layer.

Downloaded from https://www.science.org at Shanghai Jiao Tong University on May 12, 2026

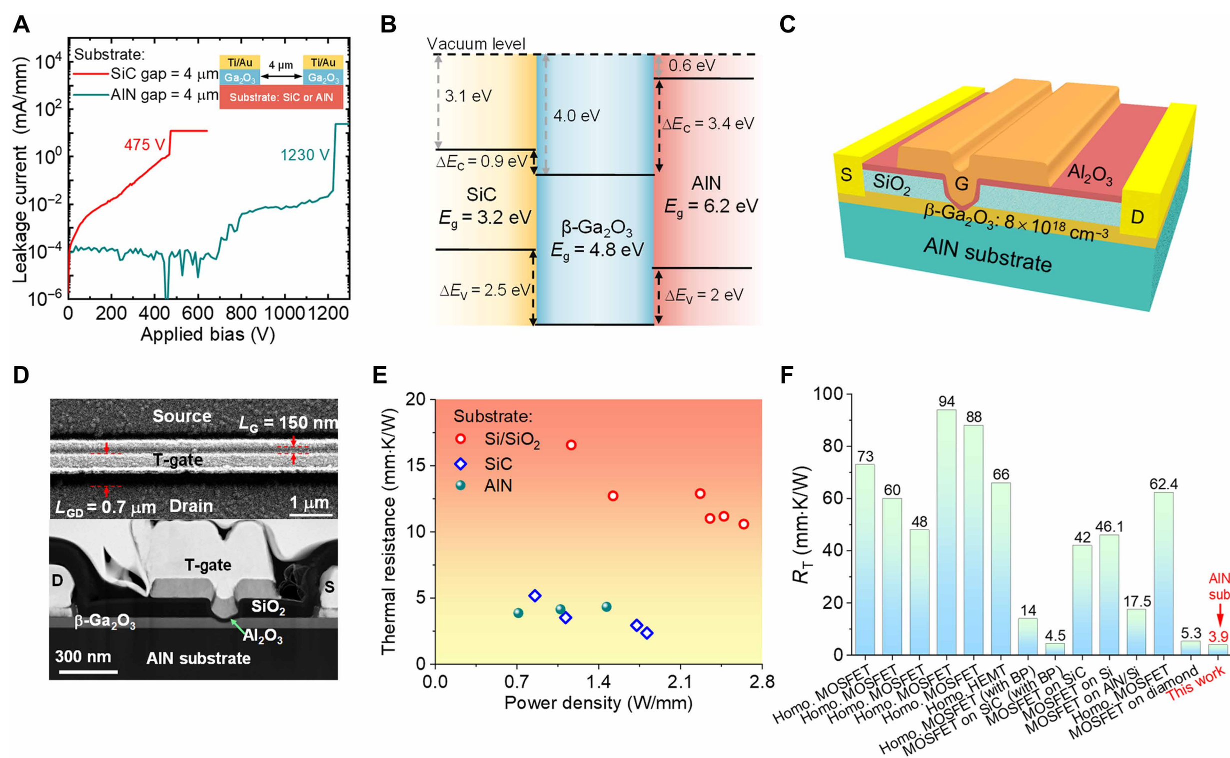

Fig. 2. Electrical and thermal properties of the hetero-UWBG platform and device design. (**A**) Leakage current characteristics between two mesa structures fabricated on the β-Ga_2O_3 on the AlN sample and the β-Ga_2O_3 on the SiC sample, revealing a 2.5 times higher breakdown voltage in the β-Ga_2O_3 on the AlN sample. (**B**) Band alignment of SiC, β-Ga_2O_3, and AlN, where a large conduction band discontinuity of 3.4 eV is presented between β-Ga_2O_3 and AlN. (**C**) Cross-sectional schematic image of β-Ga_2O_3 rf power MOSFETs on the AlN substrate. (**D**) Top-view SEM and cross-sectional TEM images of a T-gate shaped β-Ga_2O_3 rf power MOSFET with L_G = 150 nm and a gated channel thickness of 30 nm. (**E**) Extracted thermal resistance (R_T) versus dc power density of identical-geometry Ga_2O_3 MOSFETs fabricated on SiO_2/Si, SiC, and AlN substrates; the same heterogeneous integration process is applied to three substrates. (**F**) R_T benchmark for this work and other reported Ga_2O_3 transistors on a variety of substrates. Data from refs. (*17*, *26*, *32*–*38*).

Device characterization

Figure 3A shows the output characteristics (I_D-V_{DS}) of a representative Ga_2O_3-on-AlN rf power MOSFET, revealing a maximum I_D of 1.05 A/mm. Log-scale transfer characteristic (I_D-V_{GS}-I_G) at V_{DS} = 10 V is displayed in Fig. 3B, showing a subthreshold slope (SS) of 250 mV/dec and high on/off ratio of 5×10^9. Linear-scale I_D-V_{GS}-g_m (transconductance) characteristics are shown in Fig. 3C at a V_{DS} of 1/10/20 V, revealing a maximum $g_{m,max}$ of 90 mS/mm extracted at V_{DS} = 20 V. Benefited from the excellent gate control and channel electron confinement (fig. S4), the g_m remains 80% of the peak value across a wide V_{GS} range of 8.7 V (i.e., V_{GS} from −5.1 to 3.6 V), suggesting a high linearity.

Pulse *I*-*V* measurement is widely used to characterize device dynamic characteristics and identify possible degradation induced by carrier trapping. Figure 3D presents the gate-lag and drain-lag pulse I_D-V_{DS} measurements at three different quiescent bias points (V_{GSQ}, V_{DSQ}) = (0 V, 0 V), (−12 V, 0 V), and (−12 V, 25 V), which represent the cold channel, gate pulse, and drain pulse scenarios, respectively. These measurements are performed at a pulse period of 5 μs, duty cycle of 1%, and V_{GS} = 0 V. Compared with dc characteristics, the pulsed characteristics under three conditions show nearly no dispersion up to a high V_{DS} = 25 V, validating the minimal carrier trapping in the device structure and the suppression of the SHE (standard hydrogen electrode). As a comparison, a nearly identical Ga_2O_3 device is fabricated on a Ga_2O_3-on-SiC wafer that is produced by the H-implanted ion cutting (*15*), which is found to suffer from considerable current collapse in pulse *I*-*V* measurement, with the details illustrated in fig. S5. This comparison manifests the advantage of the implantation-free integration process on achieving superior device dynamic characteristics.

Three-terminal off-state breakdown characteristics of β-Ga_2O_3 rf power MOSFETs fabricated on SiC and AlN substrates are shown in Fig. 3E. Ga_2O_3-on-AlN devices achieve a *BV* of 216 and 354 V for a L_{GD} = 0.7 and 1.1 μm, respectively, rendering an averaged breakdown field (E_{ave}) of ~3 MV/cm. The faster increase in off-state drain current observed between V_{DS} = 150 and 200 V is most likely attributed to field-enhanced leakage mediated by carrier traps within the heavily doped Ga_2O_3 and at the AlN/Ga_2O_3 interface. Under a certain high voltage bias, the intense electric field in this region promotes emission from those traps via mechanisms such as Poole-Frenkel conduction, leading to increased leakage before catastrophic breakdown. A similar trap-mediated current hump has also been reported in power devices based on other materials such as gallium nitride (*39*). Further minimization of these defects includes piranha surface treatments to repair the bonded interface and annealing treatments to heal the heavily doped Ga_2O_3. In contrast, Ga_2O_3-on-SiC devices only achieve a *BV* = 168 V at a L_{GD} = 0.8 μm, corresponding to an E_{ave} of 2 MV/cm. The enhanced *BV* is further explained by physics-based technology computer-aided design (TCAD) simulations. The simulation models are described in the Materials and

Downloaded from https://www.science.org at Shanghai Jiao Tong University on May 12, 2026

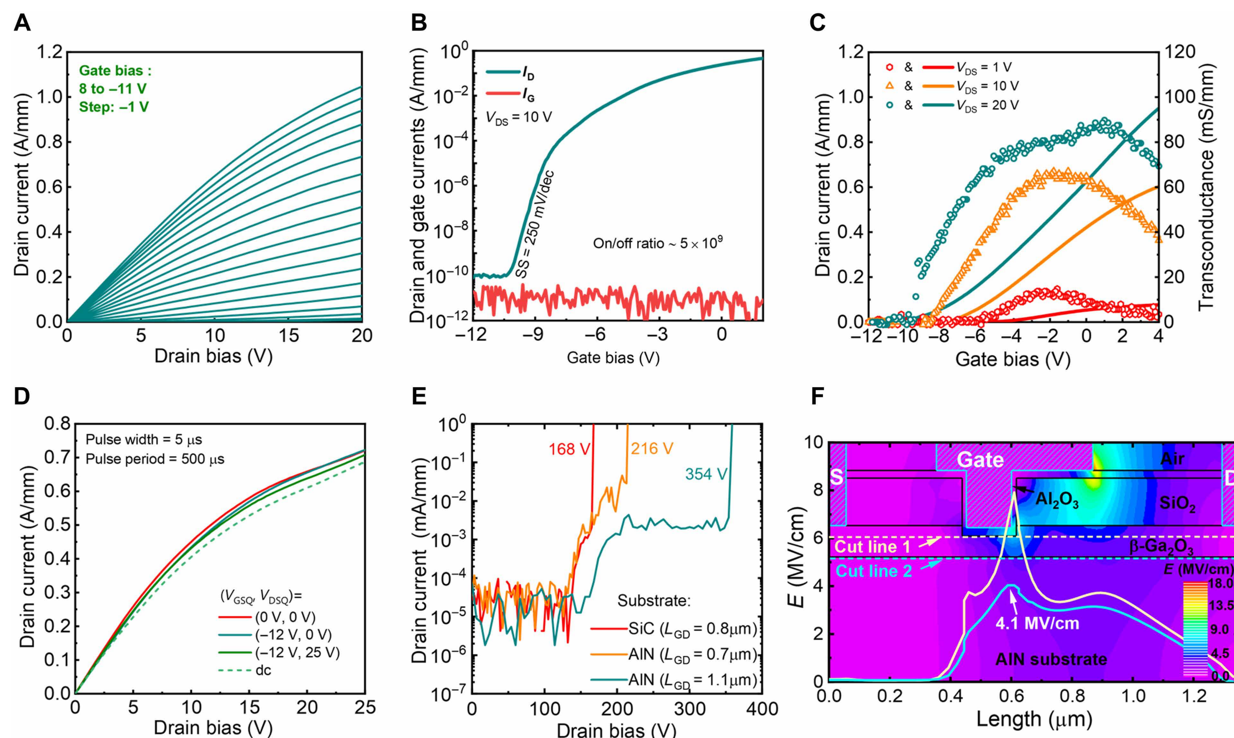

Fig. 3. dc characteristics of the Ga_2O_3-on-AlN MOSFET. (**A**) Linear-scale I_D-V_{DS} of a representative Ga_2O_3-on-AlN MOSFET with L_G = 300 nm. (**B**) Log-scale I_D-V_{GS}-I_G characteristics at V_{DS} = 10 V and (**C**) linear-scale I_D-V_{GS}-g_m characteristics at V_{DS} = 1/10/20 V of the same device. (**D**) Pulsed I_D-V_{DS} characteristics of the device under three quiescent bias conditions with 5-μs pulse width, 1% duty cycle, and V_{GS} = 0 V. (**E**) Three-terminal off-state leakage current and breakdown characteristics of β-Ga_2O_3 MOSFETs fabricated on SiC and AlN substrates. (**F**) Simulated electric field contour within the Ga_2O_3-on-AlN MOSFET structure at a device breakdown voltage of 216 V, as well as the electric field profiles along the two cutlines in the Ga_2O_3 channel and AlN substrate. Although the breakdown occurs in Ga_2O_3, a high field of 4.1 MV/cm is present in the AlN substrate; if such a substrate field cannot be withstood by the substrate material, premature breakdown will occur in the substrate.

Methods section. The simulated electric field contour and extracted field profile along two cutlines are presented in Fig. 3F and fig. S6 for Ga_2O_3-on-AlN and Ga_2O_3-on-SiC devices, respectively. The simulation reveals that the BV of Ga_2O_3-on-SiC device is limited by the peak electric field in the SiC substrate. In Ga_2O_3-on-AlN devices, the substrate electric field is much lower than the E_C of AlN, thereby eliminating the premature substrate breakdown and allowing device to exploit the high E_C of Ga_2O_3 in the channel region.

Small-signal rf characteristics of β-Ga_2O_3 rf MOSFET with L_G = 300 nm is shown in Fig. 4A, when the device is biased at V_{DS} = 45 V and V_{GS} = 0 V. Standard off-wafer line-reflect-reflect-match (LRRM) calibration and pad-only parasitic from an on-wafer open structure are used to de-embed the as measured S-parameters. The f_T is determined to be 23.8 GHz, and a f_{max} of 90 GHz is determined by a conservative −20 dB/dec extrapolation slope from the maximum available gain/maximum stable gain (MAG/MSG). The $f_T \times V_{DS}$ is determined to be ~1 THz·V. The f_T/f_{max} dependence on the V_{DS} is displayed in Fig. 4B. The f_T increases with V_{DS} and saturates at V_{DS} = 25~30 V, which is ascribed to the acceleration of electron velocity by electric field and the subsequent saturation. The f_{max} also increases with V_{DS} due to the reduced gate to drain capacitance because of the enhanced depletion. This can be understood by the analytical model $f_{max} = 0.5f_T/(2\pi f_T \times R_g \times C_{gd} + R_g \times g_{ds})^{0.5}$, where C_{gd} and g_{ds} are gates to drain depletion capacitance and output conductance, respectively (40). The enhanced f_T/f_{max} at high V_{DS} benefits the amplifiers in achieving a higher gain. The f_T/f_{max} dependence on V_{GS} is summarized in fig. S7. Because of the flat g_m, both f_T and f_{max} show weak dependence on V_{GS}, suggesting a wide gate drive window for high-frequency operation.

The microwave noise performance of β-Ga_2O_3 MOSFET with L_G = 300 nm is summarized in section S9 of the Supplementary Materials. The minimal noise figure (NF_{min}) is extracted to be ~1.1 dB at f = 8 GHz. By further scaling the L_G to 150 nm at a V_{DS} = 20 V, the NF_{min} is reduced to ~0.48 dB at f = 8 GHz, as shown in fig. S8. This NF_{min} reduction is ascribed to the higher carrier velocity underneath the gate and much lower L_G, which can be understood by the relation $NF_{min} \sim f \times (I_D L_G/E_C)^{0.5} \times (\nu_{sat})^{-1} \times (R_S + R_G)^{0.5}$, with the relation derivation illustrated in section S10 of the Supplementary Materials, where the R_S and R_G are the source and gate resistance, respectively (40). The optimal noise reflection coefficient $|\Gamma_{opt}|$ and phase angle $\angle\Gamma_{opt}$ are displayed in fig. S10. The $|\Gamma_{opt}|$ and $\angle|\Gamma_{opt}|$ are measured to be 0.8 and 24° at f = 8 GHz, respectively. The as-measured noise parameters for representative device are shown in fig. S11. The NF_{min} is found to decrease at increased V_{DS} due to higher g_m and electron velocity.

The linearity performance of a β-Ga_2O_3 rf power MOSFET at V_{DS} = 15 V is characterized by two-tone load-pull input power (P_{in}) sweeps at f = 2 GHz. Figure 4C shows the measured output third-order intercept point (OIP3) and power gain (G_a) versus the P_{in}. Benefited from the flat g_m at high V_{DS}, a high OIP3 of 28 dBm and G_a = 20.5 dB are extracted. This reports the linearity performance in rf power MOSFETs based on either UWBG semiconductors or oxide semiconductors.

Downloaded from https://www.science.org at Shanghai Jiao Tong University on May 12, 2026

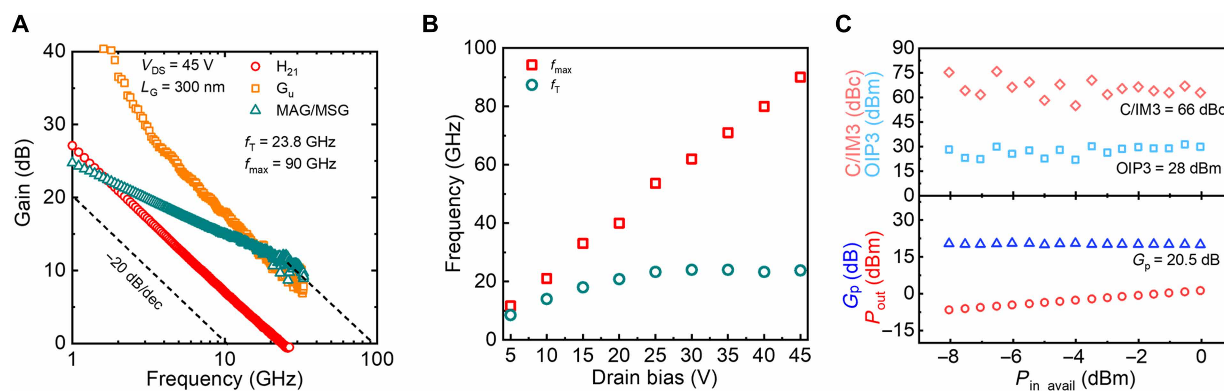

Fig. 4. Small-signal rf characteristics and linearity characteristics of the Ga_2O_3-on-AlN MOSFET. (**A**) Small-signal gain characteristics of a Ga_2O_3-on-AlN MOSFET with L_G = 300 nm when biased at V_{DS} = 45 V and at the V_{GS} corresponding to the peak g_m and (**B**) extracted f_T and f_{max} versus V_{DS}. A f_{max} = 90 GHz is extracted. (**C**) Two-tone load-pull P_{in} sweeps at f = 2 GHz to study the linearity of a device at V_{DS} = 15 V. A high linearity with OIP3 = 28 dBm is extracted.

Figure 5A shows the large-signal and class-AB load-pull characteristics of the β-Ga_2O_3 rf MOSFET measured at f = 2 GHz and V_{DS} = 30 V. The input and output are matched, and the input signal is under pulse condition with a pulse width of 100 μs and duty cycle of 10%. By sweeping the P_{in} from 12 to 23 dBm, the P_{out} and PAE first increases and then saturates. Maximum P_{out} = 4.6 W/mm and PAE = 50.5% are achieved. The dependence of P_{out} and PAE on V_{DS} is summarized in Fig. 5B, revealing a P_{out} growing with V_{DS} with a relatively constant PAE. By further increasing V_{DS} to 50 V, the measured P_{out} remains saturated at around 4 W/mm. This P_{out} saturation is probably attributed to the current collapse under high V_{DS} bias induced by the traps located at the Ga_2O_3/AlN and Ga_2O_3/passivation layer interfaces. Further process refinement, such as piranha solution treatment and annealing that have been reported to be effective in interface trap minimization (*41*), could be explored to improve P_{out}. Last, the C-band (6 GHz) load-pull measurement result of a device at V_{DS} = 45 V is displayed as Fig. 5C, revealing a P_{out} = 4.1 W/mm. Similar P_{out} and PAE versus V_{DS} trends at 6 GHz are identical to that of 2 GHz, as shown in Fig. 5D. These results demonstrate high P_{out} and PAE performance under a wide range of power and frequency in large-signal operation.

Performance benchmarking and conclusion

Among the UWBG rf power transistors reported in β-Ga_2O_3 (*6*, *13*, *14*, *18*, *19*, *42*–*45*), high Al-composition $Al_xGa_{1-x}N$ ($x \geq 50\%$) (*46*), and diamond (*47*–*53*), the Ga_2O_3-on-AlN transistor fabricated in this work presents the highest P_{out} and PAE (Fig. 6A). At 2 GHz, the P_{out} and PAE is six- and threefold higher than the best reports in Ga_2O_3 transistors on the native substrate (*13*), respectively, as well as 1.5- and twofold higher than Ga_2O_3-on-SiC devices (*19*, *45*). The P_{out} advantage over Ga_2O_3-on-SiC devices (*19*, *45*) expands to 2~4 times at the higher frequency of 4~6 GHz. It should be noted that the P_{out} performance of Ga_2O_3 rf transistors still lags behind that of GaN high-electron-mobility transistors (HEMTs) (*54*–*59*), primarily due to the still-maturing material and device process technologies considering the early stage of development. Whereas the introduction of heterogeneous integration has enabled substantial advances in the Ga_2O_3 rf FET, P_{out} improvement from 0.8 to over 4 W/mm with PAE increased from <20 to 50%. In addition, despite an inferior P_{out}, the Ga_2O_3 rf FET has shown a higher average electric field than that in GaN HEMTs (usually around 1 MV/cm). Moving forward, we believe that the rf performance of hetero-UWBG devices can be further advanced along two pathways: (i) interface engineering to suppress the interfacial dielectric layer formation and reduce interfacial trap density and (ii) device optimizations to downscale gate, reduce ohmic contact resistance, and adopt multidimensional architectures such as FinFETs and multichannel designs (*60*).

In addition to UWBG semiconductors, β-Ga_2O_3 devices also belong to another device category—oxide rf transistors, which are widely used in back-end-of-line (BEOL) and small-signal applications (*61*–*66*). Here, we benchmark the small-signal performance of our device with representative GaN rf transistors (*57*, *58*, *67*–*71*) and the state-of-the-art oxide rf transistors reported in β-Ga_2O_3 (*6*, *11*–*14*, *18*, *19*, *42*–*45*, *72*, *73*), In_2O_3 (*61*, *62*), ITO (indium tin oxide) (*63*, *64*), IGZO (indium gallium zinc oxide) (*65*), and IZO (indium zinc oxide) (*66*) for the trade-off between f_{max} and $f_T \times V_{DS}$, as shown in Fig. 6B. Our Ga_2O_3-on-AlN rf transistor has reached a record-high $f_T \times V_{DS}$ = 1 THz·V and f_{max} = 90 GHz, respectively.

Last, to showcase the potential of Ga_2O_3-on-AlN rf MOSFET in not only high-power but also low-noise amplifiers, the device is benchmarked with state-of-the-art low-noise X-band transistors reported in GaAs, InP, GaN, and diamond, as shown in fig. S12. The NF_{min} = 0.48 dB is one of the lowest values among these X-band transistors, validating the high quality in materials and interfaces in the heterogeneously integrated Ga_2O_3-on-AlN structure.

In summary, this work presents a Ga_2O_3-on-AlN heterogeneously integrated platform for rf power devices, which can leverage the complementary electrical and thermal properties of multiple UWBG materials. The integration method combines exfoliated transfer and wafer-scale bonding, obviating the ion implantation and interfacial oxide required in many conventional methods, at the same time enabling a uniform geometry of the arrayed thin films with the total size scalable to the wafer level. The Ga_2O_3-on-AlN rf transistor leverages the high potential barrier offered by the AlN/Ga_2O_3 junction to realize tight gate control and gate length scalability in a highly doped Ga_2O_3 channel. In addition, the high E_C of the AlN substrate eliminates the premature substrate breakdown. These synergistic advances in the material, process, and device enable impressive frequency and power performance, including an average electric field over 3 MV/cm, a f_T/f_{max} of 23.8/90 GHz, a P_{out} of 4.1 to 4.6 W/mm

Downloaded from https://www.science.org at Shanghai Jiao Tong University on May 12, 2026

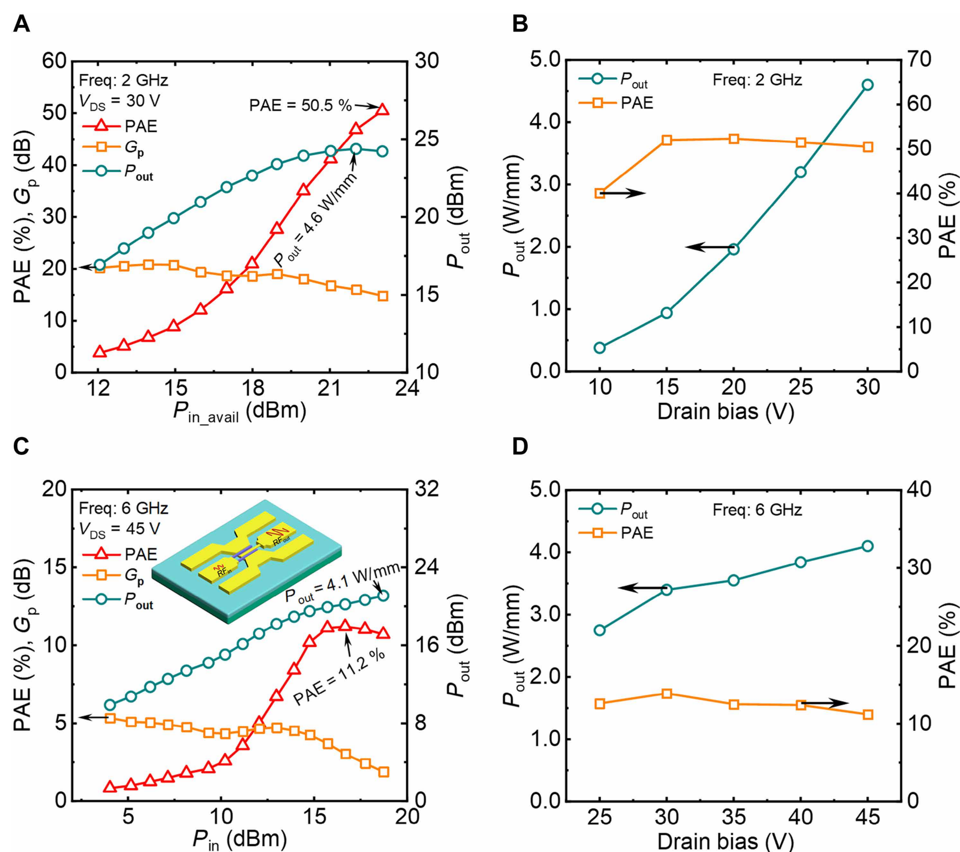

Fig. 5. Large-signal rf characteristics of the Ga_2O_3-on-AlN MOSFET. (**A**) Large-signal performance of a Ga_2O_3-on-AlN MOSFET with $L_{GS}/L_{GD}/L_G$ = 400/700/300 nm and $W_G = 2 \times 30$ μm and the (**B**) extracted P_{out} and PAE dependence on V_{DS}. The device is biased at class-AB condition with a frequency of 2 GHz, pulse width of 100 μs, and duty cycle of 10%. A record P_{out} = 4.6 W/mm at 2 GHz and PAE = 50.5% are achieved. (**C**) Large-signal class-AB performance of a Ga_2O_3-on-AlN MOSFET with $L_{GS}/L_{GD}/L_G$ = 400/700/300 nm and $W_G = 2 \times 15$ μm, with a power sweep at f = 6 GHz and V_{DS} = 45 V. Inset: Schematic of a Ga_2O_3-on-AlN MOSFET for an amplifier with rf signal amplification (**D**) P_{out} and PAE dependence on V_{DS} from 25 to 45 V at f = 6 GHz. A P_{out} = 4.1 W/mm at 6 GHz is extracted.

at 2 to 6 GHz, and a NF_{min} of 0.48 dB at 8 GHz, with the P_{out} being the highest in all UWBG rf devices and the noise among the one of the lowest in all representative X-band rf devices. These results suggest great potential of the heterogeneous UWBG platform for high-frequency, high-power, and low-noise rf electronics.

MATERIALS AND METHODS

Heterogeneous integration via exfoliation, layer transfer, and bonding

The (-201) β-Ga_2O_3 and Al-face AlN substrates are grown by edge-defined melt-grown and high-temperature high-pressure physical vapor transport (PVT) methods, respectively. The (-201) β-Ga_2O_3 (5 mm by 5 mm by 0.5 mm) and AlN (1 inch) substrates are both pretreated by piranha solution followed by buffered oxide etch (BOE) etch and water rinse. The β-Ga_2O_3 cleaved edge is manually bonded to the blue tape and forms an array. The initial thickness of the exfoliated β-Ga_2O_3 belts is ~10 μm. The thickness of the β-Ga_2O_3 belts or films on blue tape is reduced by multiple bonding processes as repeated peeling and re-bonding to fresh tape progressively remove sublayers through weak interfacial adhesion at cleavage planes. The ambient condition is high-purity nitrogen environment to avoid pollution. Thickness reduction per cycle (~20 to 30%) is monitored via cross-sectional SEM. When the thickness is reduced to ~500 nm, the blue tape is placed above a Si carrier wafer and graphite gasket with β-Ga_2O_3 side untouched. The AlN substrate is mounted at the top and then placed upside down into the bonding chamber. Room-temperature bonding with duration of 3 hours at a force of 3375 N is implemented by the SUSS MicroTec semiautomatic wafer bonder (SB6-8GEN2). The final thickness of the β-Ga_2O_3 films on the AlN substrate is around 400 nm.

Fabrication of UWB Ga_2O_3-on-AlN rf power MOSFETs

Device full fabrication processes are summarized in fig. S13. After dry etching the β-Ga_2O_3 thin film, the final Ga_2O_3 thickness is reduced to ~60 nm and another piranha treatment is implemented to smooth the surface and partially repair the surface damage. Mesa isolation is realized by BCl_3/Ar dry etching. The low-resistance alloyed ohmic contact is formed by evaporating Ti/Au (60/120 nm) followed by rapid thermal annealing at 450°C for 2 min. The contact resistance is measured to be 0.45 ohm·mm. A 100-nm SiO_2 layer is deposited on the surface by plasma-enhanced chemical vapor deposition (PECVD) at 200°C. The channel recess region is formed by electron-beam lithography (EBL), which is followed by inductively

Downloaded from https://www.science.org at Shanghai Jiao Tong University on May 12, 2026

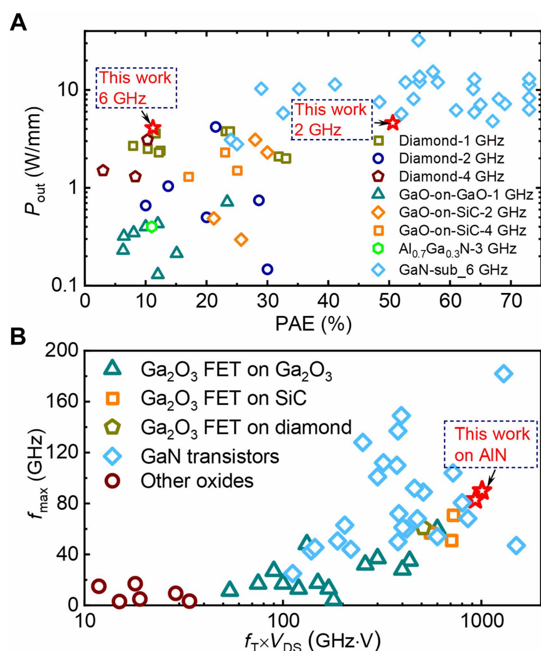

Fig. 6. Benchmark of the rf metrics for the Ga_2O_3-on-AlN MOSFET against the state-of-the-art rf transistors. (**A**) P_{out} versus PAE of rf transistors reported in various UWBG material platforms, including diamond, Ga_2O_3-on-Ga_2O_3, Ga_2O_3-on-SiC, $Al_{0.7}Ga_{0.3}N$, and representative GaN rf transistors, reported at a frequency from 1 to 6 GHz. Data from refs. (*6*, *13*, *14*, *18*, *19*, *42*–*59*). (**B**) f_{max} versus $f_T \times V_{DS}$ of the best data reported in rf transistors based on various oxide materials, including Ga_2O_3, In_2O_3, ITO, IGZO, and IZO, and representative GaN rf transistors. Data from refs. (*6*, *11*–*14*, *18*, *19*, *42*–*45*, *57*, *58*, *61*–*73*). The device with $L_G/W_G/L_{GD} = 0.3/2 \times 30/0.7$ µm has $f_T = 23.3/23.8$ GHz at $V_{DS} = 40/45$ V and $BV = 216$ V.

coupled plasma reactive ion etching (ICP-RIE) of the SiO_2 layer and ~30 nm of β-Ga_2O_3 to minimize the SCE and improve f_{max} as well as power gain. Another piranha treatment for 30 s is used to repair the etch damage and smoothen recess channel. The Al_2O_3 gate dielectric is formed by atomic layer deposition (ALD) with a thickness of 20 nm at a temperature of 300°C. The T-gate is formed by EBL and Ni/Au (50/350 nm) deposition and lift-off process. Source and drain ground-signal-ground pads were formed by etching the SiO_2 layer. Identical Ga_2O_3 devices are fabricated on SiC and Si/SiO_2 substrates for comparison.

Device characterizations

The dc *I-V* and *C-V* characteristics were measured by the Keithley 4200 semiconductor analyzer systems and a Signatone probe station. Thermal resistance characterizations were performed by a transient thermal reflectance equipment with a 532-nm green light-emitting diode light source. The top surface of the gate electrode pad is gold as the thermoreflectance coefficient of gold at this wavelength is sufficiently high to enable accurate measurements. The thermoreflectance coefficient of gold was determined to be ~2.0×10^{-4} K^{-1}, which is consistent with other reports (*74*, *75*). The schematic of a transient thermal reflectance setup was displayed in fig. S14. The S-parameter small-signal measurements were performed with an Agilent PNA-X N5245B network analyzer, and large signal measurements were performed with a Maury load pull system and Cascade probes. Microwave noise characterizations were performed using a Focus Microwaves noise measurement system. The two-tone linearity performance was evaluated using the Maury Microwave's on-wafer load-pull measurement system, in which the two tones (f_1, f_2) were centered on 2 GHz (f_0) with a tone spacing of 10 MHz. The linearity, noise, and load-pull characterizations setup were described in figs. S15 to S17.

Device simulation models and parameters

In the TCAD simulation, the main physical models include the Lombardi model, Fermi-Dirac model, Shockley-Read-Hall model, Chynoweth model, and parallel electric field dependence model. The THERMCONTACT statement is adopted to specify the thermal boundary condition. The β-Ga_2O_3 impact ionization parameters of the Chynoweth model are based on the values reported in refs. (*76*, *77*). Details of these models are provided in the ATLAS user manual (*78*). Important simulation models and parameters are summarized in table S2 of the Supplementary Materials. Basic material parameters used in simulation are summarized in table S3 of the Supplementary Materials.

Downloaded from https://www.science.org at Shanghai Jiao Tong University on May 12, 2026

Supplementary Materials

This PDF file includes:
Supplementary Text
Figs. S1 to S17
Tables S1 to S3
References

REFERENCES AND NOTES

1. J. W. Palmour, S. T. Sheppard, R. P. Smith, S. T. Allen, W. L. Pribble, T. J. Smith, Z. Ring, J. J. Sumakeris, A. W. Saxler, J. W. Milligan, "Wide bandgap semiconductor devices and MMICs for RF power applications," in *International Electron Devices Meeting. Technical Digest* (*Cat. No. 01CH37224*) (IEEE, 2001), pp. 14–17.
2. J. Y. Tsao, S. Chowdhury, M. A. Hollis, D. Jena, N. M. Johnson, K. A. Jones, R. J. Kaplar, S. Rajan, C. G. Van de Walle, E. Bellotti, C. L. Chua, R. Collazo, M. E. Coltrin, J. A. Cooper, K. R. Evans, S. Graham, T. A. Grotjohn, E. R. Heller, M. Higashiwaki, M. S. Islam, P. W. Juodawlkis, M. A. Khan, A. D. Koehler, J. H. Leach, U. K. Mishra, R. J. Nemanich, R. C. N. Pilawa-Podgurski, J. B. Shealy, Z. Sitar, M. J. Tadjer, A. F. Witulski, M. Wraback, J. A. Simmons, Ultrawide-bandgap semiconductors: Research opportunities and challenges. *Adv. Electron. Mater.* **4**, 1600501 (2018).
3. Y. Zhang, A. Zubair, Z. Liu, M. Xiao, J. Perozek, Y. Ma, T. Palacios, GaN FinFETs and trigate devices for power and RF applications: Review and perspective. *Semicond. Sci. Technol.* **36**, 054001 (2021).
4. S. Pavlidis, G. Medwig, M. Thomas, Ultrawide-bandgap semiconductors for high-frequency devices. *IEEE Microw. Mag.* **25**, 68–79 (2024).
5. M. Higashiwaki, G. H. Jessen, Guest Editorial: The dawn of gallium oxide microelectronics. *Appl. Phys. Lett.* **112**, 60401 (2018).
6. N. Moser, K. Liddy, A. Islam, N. Miller, K. Leedy, T. Asel, S. Mou, A. Green, K. Chabak, Toward high voltage radio frequency devices in β-Ga_2O_3. *Appl. Phys. Lett.* **117**, 242101 (2020).
7. M. Porter, X. Yang, H. Gong, B. Wang, Z. Yang, Y. Zhang, Switching figure-of-merit, optimal design, and power loss limit of (ultra-) wide bandgap power devices: A perspective. *Appl. Phys. Lett.* **125**, 110501 (2024).
8. N. Donato, F. Udrea, Static and dynamic effects of the incomplete ionization in superjunction devices. *IEEE Trans. Electron Devices* **65**, 4469–4475 (2018).
9. T. Ohtsuki, T. Kamimura, M. Higashiwaki, Suppression of drain current leakage and short-channel effect in lateral Ga_2O_3 RF MOSFETs using $(Al_xGa_{1-x})_2O_3$ back-barrier. *IEEE Electron Device Lett.* **44**, 1829–1832 (2023).
10. X.-C. Wang, X.-L. Lu, Y.-L. He, F. Zhang, Y. Shao, P. Liu, Z.-N. Zhang, X.-F. Zheng, W.-W. Chen, L. Wang, J. Yang, X.-H. Ma, Y. Hao, Quasi-2D high mobility channel E-mode β-Ga_2O_3 MOSFET with Johnson FOM of 7.56 THz·V. *Appl. Phys. Lett.* **125**, 63505 (2024).
11. C. N. Saha, A. Vaidya, N. J. Nipu, L. Meng, D. S. Yu, H. Zhao, U. Singisetti, Thin channel Ga_2O_3 MOSFET with 55 GHz f_{MAX} and >100 V breakdown. *Appl. Phys. Lett.* **125**, 62101 (2024).
12. K. D. Chabak, D. E. Walker, A. J. Green, A. Crespo, M. Lindquist, K. Leedy, S. Tetlak, R. Gilbert, N. A. Moser, G. Jessen, "Sub-micron gallium oxide radio frequency field-effect transistors," in *2018 IEEE MTT-S International Microwave Workshop Series on Advanced Materials and Processes for RF and THz Applications* (*IMWS-AMP*) (IEEE, 2018), pp. 1–3.

13. N. A. Moser, T. Asel, K. J. Liddy, M. Lindquist, N. C. Miller, S. Mou, A. Neal, D. E. Walker, S. Tetlak, K. D. Leedy, G. H. Jessen, A. J. Green, K. D. Chabak, Pulsed power performance of β-Ga_2O_3 MOSFETs at L-band. *IEEE Electron Device Lett.* **41**, 989–992 (2020).
14. Y. Lv, H. Liu, Y. Wang, X. Fu, C. Ma, X. Song, X. Zhou, Y. Zhang, P. Dong, H. Du, S. Liang, T. Han, J. Zhang, Z. Feng, H. Zhou, S. Cai, Y. Hao, Oxygen annealing impact on β-Ga_2O_3 MOSFETs: Improved pinch-off characteristic and output power density. *Appl. Phys. Lett.* **117**, 133503 (2020).
15. W. Xu, Y. Wang, T. You, X. Ou, G. Han, H. Hu, S. Zhang, F. Mu, T. Suga, Y. Zhang, Y. Hao, X. Wang, "First demonstration of waferscale heterogeneous integration of Ga_2O_3 MOSFETs on SiC and Si substrates by ion-cutting process," in *2019 IEEE International Electron Devices Meeting* (*IEDM*) (IEEE, 2019), pp. 12–15.
16. W. Xu, T. Zhao, L. Zhang, K. Liu, H. Sun, Z. Qu, T. You, A. Yi, K. Huang, G. Han, F. Mu, T. Suga, X. Ou, Y. Hao, Thermal transport properties of β-Ga_2O_3 thin films on Si and SiC substrates fabricated by an ion-cutting process. *ACS Appl. Electron. Mater.* **6**, 1710–1717 (2024).
17. Y. Song, D. Shoemaker, J. H. Leach, C. M. Gray, H.-L. Huang, A. Bhattacharyya, Y. Zhang, C. U. Gonzalez-Valle, T. Hess, S. Zhukovsky, K. Ferri, R. M. Lavelle, C. Perez, D. W. Snyder, J.-P. Maria, B. Ramos-Alvarado, X. Wang, S. Krishnamoorthy, J. Hwang, B. M. Foley, S. Choi, Ga_2O_3-on-SiC composite wafer for thermal management of ultrawide bandgap electronics. *ACS Appl. Mater. Interfaces* **13**, 40817–40829 (2021).
18. X. Yu, W. Xu, Y. Wang, B. Qiao, R. Shen, J. Zhou, Z. Li, T. You, Z. Shen, K. Zhang, F.-F. Ren, D. Tang, X. Ou, G. Han, Y. Kong, T. Chen, S. Gu, Y. Zheng, J. Ye, R. Zhang, Heterointegrated Ga_2O_3-on-SiC RF MOSFETs with f_T/f_{max} of 47/51 GHz by ion-cutting process. *IEEE Electron Device Lett.* **44**, 1951–1954 (2023).
19. M. Zhou, H. Zhou, S. Mengwei, G. Gao, X. Chen, X. Zhu, K. Dang, M. Peijun, M. Xiaohua, X. Zheng, Z. Liu, J. Zhang, Y. Zhang, Y. Hao, "71 GHz-f_{max} β-Ga_2O_3-on-SiC RF Power MOSFETs with Record P_{out}= 3.1 W/mm and PAE= 50.8% at 2 GHz, P_{out}= 2.3 W/mm at 4 GHz, and Low Microwave Noise Figure," in *2024 IEEE Symposium on VLSI Technology and Circuits* (*VLSI Technology and Circuits*) (IEEE, 2024), pp. 1–2.
20. J. Montes, C. Yang, H. Fu, T.-H. Yang, K. Fu, H. Chen, J. Zhou, X. Huang, Y. Zhao, Demonstration of mechanically exfoliated β-Ga_2O_3/GaN pn heterojunction. *Appl. Phys. Lett.* **114**, 162103 (2019).
21. Z. Cheng, L. Yates, J. Shi, M. J. Tadjer, K. D. Hobart, S. Graham, Thermal conductance across β-Ga_2O_3-diamond van der Waals heterogeneous interfaces. *APL Mater.* **7**, 31118 (2019).
22. J. Noh, S. Alajlouni, M. J. Tadjer, J. C. Culbertson, H. Bae, M. Si, H. Zhou, P. A. Bermel, A. Shakouri, P. D. Ye, High performance β-Ga_2O_3 nano-membrane field effect transistors on a high thermal conductivity diamond substrate. *IEEE J. Electron Devices Soc.* **7**, 914–918 (2019).
23. T. Matsumae, Y. Kurashima, H. Umezawa, K. Tanaka, T. Ito, H. Watanabe, H. Takagi, Low-temperature direct bonding of β-Ga_2O_3 and diamond substrates under atmospheric conditions. *Appl. Phys. Lett.* **116**, 141602 (2020).
24. Y. Zheng, E. Swinnich, J.-H. Seo, Investigation of thermal properties of β-Ga_2O_3 nanomembranes on diamond heterostructure using Raman thermometry. *ECS J. Solid State Sci. Technol.* **9**, 055007 (2020).
25. H. Zhou, K. Maize, J. Noh, A. Shakouri, P. D. Ye, Thermodynamic studies of β-Ga_2O_3 nanomembrane field-effect transistors on a sapphire substrate. *ACS Omega* **2**, 7723–7729 (2017).
26. Z. Qu, Y. Xie, T. Zhao, W. Xu, Y. He, Y. Xu, H. Sun, T. You, G. Han, Y. Hao, X. Ou, Extremely low thermal resistance of β-Ga_2O_3 MOSFETs by co-integrated design of substrate engineering and device packaging. *ACS Appl. Mater. Interfaces* **16**, 57816–57823 (2024).
27. C. H. Lin, N. Hatta, K. Konishi, S. Watanabe, A. Kuramata, K. Yagi, M. Higashiwaki, Single-crystal-Ga_2O_3/polycrystalline-SiC bonded substrate with low thermal and electrical resistances at the heterointerface. *Appl. Phys. Lett.* **114**, 32103 (2019).
28. Y. Song, A. Bhattacharyya, A. Karim, D. Shoemaker, H.-L. Huang, S. Roy, C. M. Gray, J. H. Leach, J. Hwang, S. Krishnamoorthy, S. Choi, Ultra-wide band gap Ga_2O_3-on-SiC MOSFETs. *ACS Appl. Mater. Interfaces* **15**, 7137–7147 (2023).
29. C. Liu, Y. Wang, W. Xu, X. Jia, S. Huang, Y. Li, B. Li, Z. Luo, C. Fang, Y. Liu, T. You, X. Ou, Y. Hao, G. Han, Unique bias stress instability of heterogeneous Ga_2O_3-on-SiC MOSFET. *IEEE Electron Device Lett.* **44**, 1256–1259 (2023).
30. M. E. Levinshtein, S. L. Rumyantsev, M. S. Shur, *Properties of Advanced Semiconductor Materials: GaN*, *AIN*, *InN*, *BN*, *SiC*, *SiGe* (John Wiley & Sons, 2001).
31. Novel Crystal Technology Inc., Novel Crystal Technology Achieves Breakthrough in Ga_2O_3 Crystal Growth, Paving Way for Larger, Higher-Quality Wafers, https://novelcrystal.co.jp/eng/2023/2340/.
32. M. H. Wong, Y. Morikawa, K. Sasaki, A. Kuramata, S. Yamakoshi, M. Higashiwaki, Characterization of channel temperature in Ga_2O_3 metal-oxide-semiconductor field-effect transistors by electrical measurements and thermal modeling. *Appl. Phys. Lett.* **109**, 193503 (2016).
33. N. A. Blumenschein, N. A. Moser, E. R. Heller, N. C. Miller, A. J. Green, A. Popp, A. Crespo, K. Leedy, M. Lindquist, T. Moule, S. Dalcanale, E. Mercado, M. Singh, J. W. Pomeroy, M. Kuball, G. Wagner, T. Paskova, J. F. Muth, K. D. Chabak, G. H. Jessen, Self-heating characterization of β-Ga_2O_3 thin-channel MOSFETs by pulsed *I–V* and Raman nanothermography. *IEEE Trans. Electron Devices* **67**, 204–211 (2020).
34. D. Lei, K. Han, Y. Wu, Z. Liu, X. Gong, High performance Ga_2O_3 metal-oxide-semiconductor field-effect transistors on an AlN/Si substrate. *IEEE J. Electron Devices Soc.* **7**, 596–600 (2019).
35. T. Moule, M. Singh, S. Karboyan, E. Mercado, S. Dalcanale, M. J. Uren, Y. Zhang, "Electrical and thermal characterisation of β-$(Al_xGa_{(1-x)})_2O_3/Ga_2O_3$ HEMTs," in *2019 International Conference on Compound Semiconductor Manufacturing Technology* (CS MANTECH, 2019).
36. T. Zhao, X. Yu, W. Xu, Y. He, Z. Qu, R. Shen, R. Wang, H. Guo, H. Sun, Z. Li, M. Zhou, T. You, X. Ou, "First Demonstration of Wafer-Level Arrayed β-Ga_2O_3 Thin Films and MOSFETs on Diamond by Transfer Printing Technology," in *2024 IEEE International Electron Devices Meeting* (*IEDM*) (IEEE, 2024), pp. 1–4.
37. B. Chatterjee, K. Zeng, C. D. Nordquist, U. Singisetti, S. Choi, Device-level thermal management of gallium oxide field-effect transistors. *IEEE Trans. Compon. Packag. Manuf. Technol.* **9**, 2352–2365 (2019).
38. J. W. Pomeroy, C. Middleton, M. Singh, S. Dalcanale, M. J. Uren, M. H. Wong, K. Sasaki, A. Kuramata, S. Yamakoshi, M. Higashiwaki, M. Kuball, Raman thermography of peak channel temperature in β-Ga^2O^3 MOSFETs. *IEEE Electron Device Lett.* **40**, 189–192 (2019).
39. J. Liu, M. Xiao, R. Zhang, S. Pidaparthi, C. Drowley, L. Baubutr, A. Edwards, H. Cui, C. Coles, Y. Zhang, Trap-mediated avalanche in large-area 1.2 kV vertical GaN pn diodes. *IEEE Electron Device Lett.* **41**, 1328–1331 (2020).
40. J. W. Chung, W. E. Hoke, E. M. Chumbes, T. Palacios, AlGaN/GaN HEMT With 300-GHz f_{max}. *IEEE Electron Device Lett.* **31**, 195–197 (2010).
41. H. Zhou, S. Alghmadi, M. Si, G. Qiu, P. D. Ye, Al_2O_3/β-Ga_2O_3 (-201) interface improvement through piranha pretreatment and post deposition annealing. *IEEE Electron Device Lett.* **37**, 1411–1414 (2016).
42. X. Yu, H. Gong, J. Zhou, Z. Shen, W. Xu, T. You, J. Wang, S. Zhang, Y. Wang, K. Zhang, R. Tao, Y. Wu, F.-F. Ren, X. Ou, Y. Kong, Z. Li, T. Chen, D. Chen, S. Gu, Y. Zheng, J. Ye, R. Zhang, High-voltage β-Ga_2O_3 RF MOSFETs with a shallowly-implanted 2DEG-like channel. *IEEE Electron Device Lett.* **44**, 1060–1063 (2023).
43. M. Singh, M. A. Casbon, M. J. Uren, J. W. Pomeroy, S. Dalcanale, S. Karboyan, P. J. Tasker, M. H. Wong, K. Sasaki, A. Kuramata, S. Yamakoshi, M. Higashiwaki, M. Kuball, Pulsed large signal RF performance of field-plated Ga_2O_3 MOSFETs. *IEEE Electron Device Lett.* **39**, 1572–1575 (2018).
44. A. J. Green, J. Speck, G. Xing, P. Moens, F. Allerstam, K. Gumaelius, T. Neyer, A. Arias-Purdue, V. Mehrotra, A. Kuramata, K. Sasaki, S. Watanabe, K. Koshi, J. Blevins, O. Bierwagen, S. Krishnamoorthy, K. Leedy, A. R. Arehart, A. T. Neal, S. Mou, S. A. Ringel, A. Kumar, A. Sharma, K. Ghosh, U. Singisetti, W. Li, K. Chabak, K. Liddy, A. Islam, S. Rajan, S. Graham, S. Choi, Z. Cheng, M. Higashiwaki, β-Gallium oxide power electronics. *APL Mater.* **10**, 029201 (2022).
45. M. Zhou, H. Zhou, S. Huang, M. Si, Y. Zhang, T. Luan, H. Yue, K. Dang, C. Wang, Z. Liu, J. Zhang, Y. Hao, "1.1 A/mm β-Ga_2O_3-on-SiC RF MOSFETs with 2.3 W/mm P_{out} and 30% PAE at 2 GHz and f_T/f_{max} of 27.6/57 GHz," in *2023 International Electron Devices Meeting* (*IEDM*) (IEEE, 2023), pp. 1–4.
46. A. G. Baca, B. A. Klein, J. R. Wendt, S. M. Lepkowski, C. D. Nordquist, A. M. Armstrong, A. A. Allerman, E. A. Douglas, R. J. Kaplar, RF performance of $Al_{0.85}Ga_{0.15}N/Al_{0.70}Ga_{0.30}N$ high electron mobility transistors with 80-nm gates. *IEEE Electron Device Lett.* **40**, 17–20 (2019).
47. T. G. Ivanov, J. Weil, P. B. Shah, A. G. Birdwell, K. Kingkeo, E. A. Viveiros, "Diamond RF Transistor Technology with f_t= 41 GHz and f_{max}= 44 GHz," in *2018 IEEE/MTT-S International Microwave Symposium-IMS* (IEEE, 2018), pp. 1461–1463.
48. S. Imanishi, K. Horikawa, N. Oi, S. Okubo, T. Kageura, A. Hiraiwa, H. Kawarada, 3.8 W/mm RF power density for ALD Al_2O_3-based two-dimensional hole gas diamond MOSFET operating at saturation velocity. *IEEE Electron Device Lett.* **40**, 279–282 (2019).
49. C. J. Zhou, J. J. Wang, J. C. Guo, C. Yu, Z. Z. He, Q. B. Liu, X. D. Gao, S. J. Cai, Z. H. Feng, Radiofrequency performance of hydrogenated diamond MOSFETs with alumina. *Appl. Phys. Lett.* **114**, 063501 (2019).
50. X. Yu, W. Hu, J. Zhou, B. Liu, T. Tao, Y. Kong, T. Chen, Y. Zheng, 1 W/mm output power density for H-terminated diamond MOSFETs with Al_2O_3/SiO_2 bi-layer passivation at 2 GHz. *IEEE J. Electron Devices Soc.* **9**, 160–164 (2021).
51. K. Kudara, S. Imanishi, A. Hiraiwa, Y. Komatsuzaki, Y. Yamaguchi, Y. Kawamura, S. Shinjo, H. Kawarada, High output power density of 2DHG diamond MOSFETs with thick ALD-Al_2O_3. *IEEE Trans. Electron Devices* **68**, 3942–3949 (2021).
52. K. Kudara, M. Arai, Y. Suzuki, A. Morishita, J. Tsunoda, A. Hiraiwa, H. Kawarada, Over 1 A/mm drain current density and 3.6 W/mm output power density in 2DHG diamond MOSFETs with highly doped regrown source/drain. *Carbon* **188**, 220–228 (2022).
53. C. Yu, C. Zhou, J. Guo, Z. He, M. Ma, H. Yu, X. Song, A. Bu, Z. Feng, Hydrogen-terminated diamond MOSFETs on (0 0 1) single crystal diamond with state of the art high RF power density. *Funct. Diam.* **2**, 64–70 (2022).
54. Y. Wu, A. Saxler, M. Moore, R. P. Smith, S. Sheppard, P. M. Chavarkar, T. Wisleder, U. K. Mishra, P. Parikh, 30-W/mm GaN HEMTs by field plate optimization. *IEEE Electron Device Lett.* **25**, 117–119 (2004).
55. Y. Okamoto, Y. Ando, K. Hataya, T. Nakayama, H. Miyamoto, T. Inoue, M. Senda, K. Hirata, M. Kosaki, N. Shibata, M. Kuzuhara, Improved power performance for a recessed-gate

Downloaded from https://www.science.org at Shanghai Jiao Tong University on May 12, 2026

AlGaN-GaN heterojunction FET with a field-modulating plate. *IEEE Trans. Microw. Theory Tech.* **52**, 2536–2540 (2004).
56. S. Kolluri, S. Keller, S. P. Denbaars, U. K. Mishra, N-polar GaN MIS-HEMTs with a 12.1-W/mm continuous-wave output power density at 4 GHz on sapphire substrate. *IEEE Electron Device Lett.* **32**, 635–637 (2011).
57. H. Lu, B. Hou, L. Yang, M. Zhang, L. Deng, M. Wu, Z. Si, S. Huang, X. Ma, Y. Hao, High RF performance GaN-on-Si HEMTs with passivation implanted termination. *IEEE Electron Device Lett.* **43**, 188–191 (2021).
58. S. Li, M. Wu, L. Yang, B. Yang, H. Sun, M. Zhang, B. Hou, H. Lu, X. Ma, Y. Hao, 15.1 W/mm power density GaN-on-GaN HEMT with high-gradient stepped-C doped buffer. *IEEE Electron Device Lett.* **46**, 365–368 (2025).
59. A. Bansal, R. Baby, A. Gowrisankar, V. S. Charan, R. Muralidharan, H. Chandrasekar, A. Sadhanala, S. Raghavan, D. N. Nath, Microwave power performance of buffer-free AlGaN/GaN MISHEMT with MOCVD grown ex situ SiN. *IEEE Trans. Electron Devices* **72**, 2226–2232 (2025).
60. Y. Zhang, F. Udrea, H. Wang, Multidimensional device architectures for efficient power electronics. *Nat. Electron.* **5**, 723–734 (2022).
61. A. Charnas, J. Anderson, J. Zhang, D. Zheng, D. Weinstein, P. D. Ye, Ultrathin indium oxide thin-film transistors with gigahertz operation frequency. *IEEE Trans. Electron Devices* **70**, 532–536 (2023).
62. D. Zheng, A. Charnas, J.-Y. Lin, J. Anderson, D. Weinstein, P. D. Ye, "Ultrathin Atomic-Layer-Deposited In_2O_3 Radio-Frequency Transistors with Record High f_T of 36 GHz and BEOL Compatibility," in *2023 IEEE Symposium on VLSI Technology and Circuits* (*VLSI Technology and Circuits*) (IEEE, 2023), pp. 1–2.
63. S. Li, M. Tian, Q. Gao, M. Wang, T. Li, Q. Hu, X. Li, Y. Wu, Nanometre-thin indium tin oxide for advanced high-performance electronics. *Nat. Mater.* **18**, 1091–1097 (2019).
64. Q. Hu, S. Zhu, C. Gu, S. Liu, M. Zeng, Y. Wu, Ultrashort 15-nm flexible radio frequency ITO transistors enduring mechanical and temperature stress. *Sci. Adv.* **8**, eade4075 (2022).
65. C. Tückmantel, U. Kalita, T. Haeger, M. Theisen, U. Pfeiffer, T. Riedl, Amorphous indium-gallium-zinc-oxide TFTs patterned by self-aligned photolithography overcoming the GHz threshold. *IEEE Electron Device Lett.* **41**, 1786–1789 (2020).
66. D. Zheng, A. Charnas, J. Anderson, H. Dou, Z. Hu, Z. Lin, Z. Zhang, J. Zhang, P.-Y. Liao, M. Si, H. Wang, D. Weinstein, P. D. Ye, "First demonstration of BEOL-compatible ultrathin atomiclayer-deposited InZnO transistors with GHz operation and record high bias-stress stability," in *2022 International Electron Devices Meeting* (*IEDM*) (IEEE, 2022), pp. 3–4.
67. J. Liu, Y. Zhou, J. Zhu, Y. Cai, K. M. Lau, K. J. Chen, DC and RF characteristics of AlGaN/GaN/InGaN/GaN double-heterojunction HEMTs. *IEEE Trans. Electron Devices* **54**, 2–10 (2007).
68. C.-W. Tsou, C.-Y. Lin, Y.-W. Lian, S. S. H. Hsu, 101-GHz InAlN/GaN HEMTs on silicon with high Johnson's figure-of-merit. *IEEE Trans. Electron Devices* **62**, 2675–2678 (2015).
69. S. Dai, Y. Zhou, Y. Zhong, K. Zhang, G. Zhu, H. Gao, Q. Sun, T. Chen, H. Yang, High f_T AlGa (In) N/GaN HEMTs grown on Si with a low gate leakage and a high ON/OFF current ratio. *IEEE Electron Device Lett.* **39**, 576–579 (2018).
70. W. Song, Z. Zheng, T. Chen, J. Wei, L. Yuan, K. J. Chen, RF linearity enhancement of GaN-on-Si HEMTs with a closely coupled double-channel structure. *IEEE Electron Device Lett.* **42**, 1116–1119 (2021).
71. Q. Yu, C. Shi, L. Yang, H. Lu, M. Zhang, M. Wu, B. Hou, F. Jia, F. Guo, X. Ma, Y. Hao, High current and linearity AlGaN/GaN/-graded-AlGaN: Si-doped/GaN heterostructure for low voltage power amplifier application. *IEEE Electron Device Lett.* **44**, 582–585 (2023).
72. T. Kamimura, Y. Nakata, M. Higashiwaki, Delay-time analysis in radio-frequency β-Ga_2O_3 field effect transistors. *Appl. Phys. Lett.* **117**, 253501 (2020).
73. A. Vaidya, C. N. Saha, U. Singisetti, Enhancement mode β-$(Al_xGa_{1-x})_2O_3/Ga_2O_3$ heterostructure FET (HFET) with high transconductance and cutoff frequency. *IEEE Electron Device Lett.* **42**, 1444–1447 (2021).
74. N. Kumar, D. Vaca, C. Joishi, Z. Xia, S. Rajan, S. Kumar, Ultrafast thermoreflectance imaging and electrothermal modeling of β-Ga_2O_3 MESFETs. *IEEE Electron Device Lett.* **41**, 641–644 (2020).
75. T. Favaloro, J.-H. Bahk, A. Shakouri, Characterization of the temperature dependence of the thermoreflectance coefficient for conductive thin films. *Rev. Sci. Instrum.* **86**, 024903 (2015).
76. K. Ghosh, U. Singisetti, Impact ionization in β-Ga_2O_3. *J. Appl. Phys.* **124**, 085707 (2018).
77. F. Zhou, H. Gong, M. Xiao, Y. Ma, Z. Wang, X. Yu, L. Li, L. Fu, H. H. Tan, Y. Yang, F.-F. Ren, S. Gu, Y. Zheng, H. Lu, R. Zhang, Y. Zhang, J. Ye, An avalanche-and-surge robust ultrawide-bandgap heterojunction for power electronics. *Nat. Commun.* **14**, 4459 (2023).
78. Silvaco, Atlas User's Manual Device Simulation Software, http://silvaco.com.
79. H. Fukui, Optimal noise figure of microwave GaAs MESFET's. *IEEE Trans. Electron Devices* **26**, 1032–1037 (1979).
80. D. Delagebeaudeuf, J. Chevrier, M. Laviron, P. Delescluse, A new relationship between the Fukui coefficient and optimal current value for low-noise operation of field-effect transistors. *IEEE Electron Device Lett.* **6**, 444–445 (1985).
81. S. Lardizabal, L. Dunleavy, W. Yau, S. Bar, "Experimental investigation of the temperature dependence of PHEMT noise parameters," in *1994 IEEE MTT-S International Microwave Symposium Digest* (*Cat. No. 94CH3389-4*) (IEEE, 1994), pp. 845–848.
82. W. Lu, V. Kumar, R. Schwindt, E. Piner, I. Adesida, DC, RF, and microwave noise performances of AlGaN/GaN HEMTs on sapphire substrates. *IEEE Trans. Microw. Theory Tech.* **50**, 2499–2504 (2002).
83. H. K. Huang, C. S. Wang, Y. Wang, C. L. Wu, C. S. Chang, Temperature effects of low noise InGaP/InGaAs/GaAs PHEMTs. *Solid State Electron.* **47**, 1989–1994 (2003).
84. J. Lee, A. Kuliev, V. Kumar, R. Schwindt, I. Adesida, Microwave noise characteristics of AlGaN/GaN HEMTs on SiC substrates for broad-band low-noise amplifiers. *IEEE Microw. Wirel. Compon. Lett.* **14**, 259–261 (2004).
85. W. Lu, J. Yang, M. A. Khan, I. Adesida, AlGaN/GaN HEMTs on SiC with over 100 GHz f_T and low microwave noise. *IEEE Trans. Electron Devices* **48**, 581–585 (2001).
86. H. Sun, A. R. Alt, H. Benedickter, C. R. Bolognesi, High-performance 0.1-μm gate AlGaN/GaN HEMTs on silicon with low-noise figure at 20 GHz. *IEEE Electron Device Lett.* **30**, 107–109 (2009).
87. J. S. Moon, D. Wong, P. Hashimoto, M. Hu, I. Milosavljevic, P. Willadsen, C. McGuire, S. Burnham, M. Micovic, M. Wetzel, D. Chow, Sub-1-dB noise figure performance of high-power field-plated GaN HEMTs. *IEEE Electron Device Lett.* **32**, 297–299 (2010).
88. Z. H. Liu, G. I. Ng, S. Arulkumaran, Y. K. T. Maung, K. L. Teo, S. C. Foo, V. Sahmuganathan, T. Xu, C. H. Lee, High microwave-noise performance of AlGaN/GaN MISHEMTs on silicon with Al_2O_3 gate insulator grown by ALD. *IEEE Electron Device Lett.* **31**, 96–98 (2010).
89. Z. H. Liu, G. I. Ng, S. Arulkumaran, Y. Maung, K. L. Teo, S. C. Foo, S. Vicknesh, Temperature-dependent microwave noise characteristics in ALD Al_2O_3/AlGaN/GaN MISHEMTs on silicon substrate. *IEEE Electron Device Lett.* **32**, 318–320 (2011).
90. T. Huang, O. Axelsson, T. N. T. Do, M. Thorsell, D. Kuylenstierna, N. Rorsman, Influence on noise performance of GaN HEMTs with in situ and low-pressure-chemical-vapor-deposition SiN_x passivation. *IEEE Trans. Electron Devices* **63**, 3887–3892 (2016).
91. X. Liu, S. Zhang, K. Wei, J. Guo, X. He, Y. Zhang, H. Yin, S. Huang, X. Chen, Y. Zheng, X. Wang, S. Ouyang, Y. Li, 0.18 dB low-noise figure at 10 GHz for GaN MIS-HEMT with plasma-enhanced atomic layer deposition SiN layer. *IEEE Electron Device Lett.* **44**, 1080–1083 (2023).
92. A. Aleksov, A. Denisenko, U. Spitzberg, W. Ebert, E. Kohn, Microwave performance of diamond surface-channel FETs. *IEEE Electron Device Lett.* **23**, 488–490 (2002).
93. C. H. Lin, X. B. Mei, Y. C. Chou, L. S. Lee, J. M. Yang, M. Y. Nishimoto, P. H. Liu, R. To, A. Cavus, R. Tsai, M. Wojtowicz, R. Lai, "Sub-mW operation of InP HEMT X-band low-noise amplifiers for low power applications," in *2009 Annual IEEE Compound Semiconductor Integrated Circuit Symposium* (IEEE, 2009), pp. 1–4.
94. L. Liu, A. R. Alt, H. Benedickter, C. R. Bolognesi, InP-HEMT X-band low-noise amplifier with ultralow 0.6-mW power consumption. *IEEE Electron Device Lett.* **33**, 209–211 (2011).
95. D. C. Ruiz, T. Saranovac, D. Han, O. Ostinelli, C. R. Bolognesi, "Impact ionization control in 50 nm low-noise high-speed InP HEMTs with InAs channel insets," in *2019 IEEE International Electron Devices Meeting* (*IEDM*) (IEEE, 2019), pp. 3–9.

Acknowledgments
Funding: The work in Xidian University was supported by the National Natural Science Foundation of China (NSFC) with the grant nos. 62222407 and 62421005 (to H.Z.). **Author contributions:** Conceptualization: Hong Zhou, Yuhao Zhang, Y.H., and Jincheng Zhang. Methodology: M.Z. and M.X. Investigation: Hong Zhou, M.Z., M.X., H.G., G.G., C.W., Yachao Zhang, K.D., Z.L., Jinfeng Zhang, HangMing Zhang, Y.W., H.W., M.S., and Jincheng Zhang. Visualization: Hong Zhou and Yuhao Zhang. Supervision: Y.H. and Jincheng Zhang. Writing—original draft: Hong Zhou and Yuhao Zhang. Writing—review and editing: Hong Zhou, M.Z., Yuhao Zhang, and Jincheng Zhang. **Competing interests:** The authors declare that they have no competing interests. **Data and materials availability:** All data needed to evaluate the conclusions in the paper are present in the paper and/or the Supplementary Materials.

Submitted 10 February 2025
Accepted 20 October 2025
Published 19 November 2025
10.1126/sciadv.adw6167

Downloaded from https://www.science.org at Shanghai Jiao Tong University on May 12, 2026

Science Advances

Heterogeneous integration of ultrawide bandgap semiconductors for radio frequency power devices

Hong Zhou, Min Zhou, Mingjie Xiang, Hehe Gong, Guangjie Gao, Chenlu Wang, Yachao Zhang, Kui Dang, Zhihong Liu, Jinfeng Zhang, HangMing Zhang, Yifan Wang, Han Wang, Mengwei Si, Yuhao Zhang, Yue Hao, and Jincheng Zhang

Sci. Adv. **11** (47), eadw6167. DOI: 10.1126/sciadv.adw6167

View the article online
https://www.science.org/doi/10.1126/sciadv.adw6167
Permissions
https://www.science.org/help/reprints-and-permissions

Downloaded from https://www.science.org at Shanghai Jiao Tong University on May 12, 2026

Use of this article is subject to the Terms of service

Science Advances (ISSN 2375-2548) is published by the American Association for the Advancement of Science. 1200 New York Avenue NW, Washington, DC 20005. The title *Science Advances* is a registered trademark of AAAS.

Copyright © 2025 The Authors, some rights reserved; exclusive licensee American Association for the Advancement of Science. No claim to original U.S. Government Works. Distributed under a Creative Commons Attribution License 4.0 (CC BY).